Applied Science and Engineering Progress, Vol. 20, No. 3, 2027, 8280

Research Article

Effect of the Synthesis Route on the Catalytic Performance of Magnetic Fe_2O_3@MOF Beads for the Heterogeneous Fenton-like Degradation of Ciprofloxacin

Mohammed Abdulsalam Kassim, Khazaal Hameed Khazaal, Omar A. Alwash*, and Rafid N.AL-Mashhadi
Scientific Research Commission, Baghdad, Iraq

Samer Al-Ajooli
Department of Petroleum Engineering, College of Engineering, Al-Naji University, Iraq

* Corresponding author. E-mail: omar.a.alwash@src.edu.iq DOI: 10.14416/j.asep.2026.08.015
Received: 25 April 2026; Revised: 20 June 2026; Accepted: 6 July 2026; Published online: 27 August 2026

Abstract
Highly effective heterogeneous Fenton-like catalysts are promising for the degradation of recalcitrant pharmaceutical contaminants from wastewater. Herein, we investigate the impact of the synthesis pathway on their catalytic activity using the as-prepared beads derived from chitosan with or without iron via two step and *in situ* synthesis, respectively. We aimed to find out the influence of the synthesis strategy on the dispersion of the nanoparticles, accessibility of the active sites and catalytic performance in the degradation of ciprofloxacin (CIP). The catalysts were characterized by SEM, TEM, XRD, FT-IR, XPS, TGA and BET analyses to understand their structural and physicochemical characteristics. From the comparative results, it can be concluded that the *in situ* synthesized Fe_2O_3@MOF-IS catalyst outperformed the others due to its improved dispersion and interaction of Fe_2O_3 nanoparticles with the porous matrix. Optimized conditions yielded a degradation rate of 91.8 % of CIP (46.3 mg L^{-1}) in 28 min, with 63.5% total organic carbon (TOC) being removed in 115 min. The degradation obeyed pseudo-first-order kinetics. The catalyst was also very stable with only a slight loss of activity after five cycles. Their increased performance is ascribed to the action of the synergistic structure of the composite in terms of efficient activation of H_2O_2 and hydroxyl radical (•OH). These results indicate that Fe_2O_3@MOF-IS is a promising and magnetically reusable catalyst that can be applied in a real wastewater treatment process.

Keywords: Advanced oxidation processes, Ciprofloxacin degradation, Fe_2O_3@MOF catalyst, Heterogeneous catalyst, Pharmaceutical wastewater treatment

1 Introduction

The extensive medical and pharmaceutical use of antibiotics has led to their widespread occurrence in aquatic environments. Ciprofloxacin (CIP) is one such compound; it is a widely used fluoroquinolone antibiotic that is highly persistent and resistant to conventional biological degradation processes [1]-[6]. Its continuous release into wastewater systems poses serious environmental risks, including the spread of antibiotic-resistant bacteria and long-term ecological toxicity [7], [8]. Therefore, the development of effective technologies for CIP degradation from wastewater is of great importance. CIP degradation has been studied with different techniques, which include adsorption, biological treatment and chemical oxidation [9]-[12]. Of these methods, advanced oxidation processes (AOPs) have gained significant interest due to their ability to produce extremely reactive species, especially hydroxyl radicals (•OH), that can non-selectively oxidize and mineralize persistent organic pollutants [13]-[17]. Fenton and Fenton-like systems are considered very efficient due to their strong oxidizing power and quite simple operation. Nevertheless, the traditional homogeneous Fenton reactions have some disadvantages, such as limited pH adaptation range, complications in catalyst recovery, and iron sludge [18]-[20].

In order to remedy these drawbacks, extensive research has focused on developing heterogeneous Fenton-like catalysts, especially supported iron oxide catalysts [21]-[25]. Although many reported catalysts

Applied Science and Engineering Progress, Vol. 20, No. 3, 2027, 8280

have some advantages, they still experienced issues such as nanoparticle agglomeration, metal leaching, and insufficient catalytic activity under practical conditions [26]-[29]. Embedding iron species in porous materials like metal-organic frameworks (MOFs) has become a promising approach to improve the dispersion, stability and catalytic activity [30]. As a widely applied support material, chitosan is a biopolymer of natural origin with a high content of amino and hydroxyl functional groups, low cost and environmental compatibility [31]-[34]. However, the effects of the synthesis method on the structural properties and catalytic activity of Fe_2O_3@MOF systems have not yet been fully investigated.

To compare the impact of the synthesis route on the structure and functionality of the catalysts, magnetic Fe_2O_3@MOF beads were prepared using chitosan in two different methods, *in situ* and two-step methods. Fe-based MOF catalysts, chitosan-supported Fe oxides and magnetic heterogeneous Fenton-like catalysts have been extensively explored for the degradation of emerging contaminants, while the synthesis strategy itself has comparatively little systematic investigation on the influence of the synthesis strategy on the architecture and catalytic performance of these catalysts. Direct comparison of in-situ formation of nanoparticles embedded in the supporting matrix with the traditional two-step assembly techniques is rare. The synthesis path determines the dispersion of the nanoparticles, the interactions between the particles and the pore space, the accessibility of the pores, the exposure of the active sites and the stability of the iron, which can have a significant effect on H_2O_2 activation efficiency and overall degradation rates. In this context, this work aims to build a structure–performance relationship between the *in situ* and two-step synthesized magnetic Fe_2O_3@MOF beads for the degradation of the pharmaceutical antibiotic ciprofloxacin, offering rational guidance to design efficient and reusable catalysts for pharmaceutical wastewater treatment.

2. Experiments

2.1 Materials and Chemicals

Various chemicals were used in this research, Iron chloride hexahydrate ($FeCl_3 \cdot 6H_2O$, 98%), chitosan flakes (80–95% deacetylated), hydrochloric acid (HCl, 36–38%), ethylene glycol (99%), sodium acetate (99%) and polyethylene glycol (PE9900, Chengdu Kelong chemical) were purchased from Sinopharm Chemical Reagent Co., Ltd; Ciprofloxacin hydrochloride (CIP, ≥ 98%), tert-butanol (99%) and p-benzoquinone (99%) were purchased from Shanghai Maclin Chemistry Co., Ltd., China. Sodium hydroxide, sodium citrate, and hydrogen peroxide (30 wt%) were provided by Shanghai Aladdin Chemistry Co., Ltd., China. All chemicals were of analytical grade and were used without further purification. All experiments used deionized water. All degradation experiments were performed under dark conditions without external light irradiation to eliminate any photocatalytic contribution

2.2 Preparation of porous magnetic Fe_2O_3@ MOF catalysts.

2.2.1 Method 1 (in situ synthesis)

The *in situ* technique consists of the synthesis of Fe_2O_3 nanoparticles inside the MOF structure by utilizing the co-precipitation of the iron ions (Eqs. (2)) [31], [35]. In short, 1.0 g of chitosan was dissolved in 40 mL of 1% acetic acid solution by using mechanical stirring; it took around 35 min before a homogeneous solution was attained. Then, 5 mL of Fe^{3+} precursor solution at various concentrations (0.25, 0.85 and 1.45 M) was subsequently poured into the chitosan solution. The resulting mixture was then added dropwise to an aqueous sodium hydroxide (1.2 M) solution containing sodium acetate (0.12 M) at 45 drops min^{-1}. On mixing with the alkaline solution, Fe_2O_3 nanoparticles were produced and embedded *in situ* into the MOF-like porous matrix, leading to composite bead-shaped spheres. The obtained macroscopic beads (3–4 mm in diameter) [36] were magnetically separated, washed many times with deionized water and ethanol, and freeze-dried in 24 h to get porous catalytic beds of Fe_2O_3@MOF. Chitosan beads without an iron precursor were also made following the same procedure for comparison. Thus, the resulting catalysts were labelled as $2Fe_2O_3$@MOF, $8Fe_2O_3$@MOF, $14Fe_2O_3$@MOF and Cs, respectively. The composition of the catalyst was determined by ICP-MS analysis after synthesis and the nomenclature used for the catalyst was based on the approximate amount of iron incorporated in the porous matrix generated by chitosan. Catalysts with loadings of 2, 8, and 14 have been used to prepare catalysts with increasingly large loadings of Fe_2O_3 and are represented by the prefixes 2, 8, and 14, respectively. This labelling system was chosen for simplicity to

differentiate the catalysts containing varying proportions of iron and for ease of comparison of the structural properties and catalytic performance of the different catalysts to be studied. The catalyst made without the addition of iron precursor was labeled Cs (pristine chitosan bead matrix).

The mechanism of the reaction can be drawn in the following way [37]:

$$Fe^{3+} + H_2O_2 \rightarrow Fe^{2+} + HO_2\bullet \quad (1)$$

$$Fe^{2+} + H_2O_2 \rightarrow Fe^{3+} + OH^- + \bullet OH \quad (2)$$

2.2.2 Method 2 (Two-step synthesis)

Two classes of catalysts can be distinguished in terms of the synthesis pathway: (i) Fe_2O_3@MOF-IS, where Fe2O3 nanoparticles are formed *in situ* within the framework, which leads to uniform dispersion and good interfacial contact; and (ii) Fe_2O_3@MOF-TS, where Fe_2O_3 nanoparticles are loaded into the framework. This classification is used throughout the manuscript. The solution was stirred using a magnetic stirrer and was used in a comparative manner.

Two-step synthesis is a technique that involves the synthesis of iron oxide nanoparticles and then their incorporation into the MOF structure. The solvothermal method of Fe_2O_3 nanoparticles synthesis was performed first. The 1.30 g of $FeCl_3.6H_2O$, 3.5 g of sodium acetate and 1.0 g of polyethylene glycol were added to 40 mL of ethylene glycol to create a dark brown solution. The solution was stirred using a magnetic stirrer and kept in a Teflon-lined stainless steel autoclave for 30 min. The autoclave was heated at 200 ° C, and then left to naturally cool to room temperature. The precipitate was collected and washed with deionized water and ethanol several times and dried at 60 ° C under vacuum, which took around 8 h [35]. In the second step, Fe_2O_3 nanoparticles were integrated with the MOF-based structure by dissolving 1g of chitosan and a sufficient amount of Fe_2O_3 nanoparticles in 40 mL of 2% acetic acid solution and stirring the mixture until a clear suspension was formed. The bead formation process was the same as that used in the *in situ* method.

2.3 Fe_2O_3@MOF catalysts characterization

The morphological, crystalline, surface chemical, thermal, and pore properties of the synthesized Fe_2O_3@MOF catalysts were characterized. The internal porous structures and surface morphologies were observed by scanning electron microscopy (SEM, SU-8020, Hitachi, Tokyo) and transmission electron microscopy (TEM, JEM-2100F, JEOL, Tokyo) before and after the above processes.

The diffraction plane was measured using X-ray diffraction (XRD, X'Pert PRO MPD, PANalytical, Netherlands) for crystalline phases and XRD patterns were recorded over the 2θ range of 10–70° at 40 kV and 40 mA with a scanning rate of 6° min^{-1} and 40 mA with a scanning rate of 6° min^{-1} (JCPDS-ICDD, 1993). The chemical functional groups were identified by the KBr pellet method using FT-IR spectroscopy (Bruker, Germany). Surface chemical states were determined by X-ray photoelectron spectroscopy (XPS, Shimadzu, Japan). All the C_1s, O_1s, and Fe_2p spectra were analyzed using CasaXPS 2.3.19. The thermal stability was analyzed by thermogravimetric analysis (TGA, STA449F3, Netzsch, Germany) at a range of 25-800 °C. The specific surface area and pore structure were determined by nitrogen adsorption-desorption analysis at 77 K (Autosorb-IQ3, Quantachrome, USA).

2.4 Reaction procedures

The reaction involved in the catalytic degradation of ciprofloxacin (CIP) in a heterogeneous Fenton-like reaction in sealed conical flasks. The Fe_2O_3@MOF catalyst (0.10 g) was first mixed in 200 mL of ciprofloxacin solution. Addition of hydrogen peroxide (H_2O_2) into the reaction system triggered the degradation reaction. The suspension was put in a water-bath shaker with a rotational speed of 200 rpm and reacted for 110 min at the required temperature. Aliquots of 3 mL were filtered at preset intervals to remove suspended particles. The starting solution concentration of ciprofloxacin was 0.095 mM (44.5 mg L^{-1}), and the concentration of the studied H_2O_2 was 0-35 mM (0, 5, 10, 18, 25 and 35 mM). The 0.5 M NaOH or H_2SO_4 solutions were used to change the initial pH of the solution of the reaction. Aliquots (1 mL) were withdrawn during the reaction and immediately quenched with 20 mL of tert-butanol to suppress further radical reactions.

2.5 Analysis methods

High performance liquid chromatography (HPLC, Agilent 1200 Series, USA) was used for the determination of the concentration of ciprofloxacin (CIP) with a UV detector. The mobile phase was 0.1

M oxalic acid, methanol and acetonitrile (66:12:22 v/v/v). Chromatographic separation was done at a flow rate of 1.0 mL min^{-1} at the column temperature of 30 °C and detection wavelength of 278 nm. TOC degradation efficiency was taken to assess the extent of mineralization of ciprofloxacin on a TOC/TN analyzer (Multi N/C 3100). The concentration of iron in the solution was measured with inductively coupled plasma mass spectrometry (ICP-MS, Agilent 7500) with a detection limit of approximately 1 ppb. Atomic absorption spectrophotometry (AAS, AA140, VARIAN) was used to measure the total iron leaching during the reaction. The potassium titanium (IV) oxalate spectrophotometric technique was used to measure the concentration of hydrogen peroxide at 400 nm [36]. The absorbance changes during the degradation process were monitored over the wavelength range of 200–700 nm using a UV–Vis spectrophotometer (Hitachi U-2900, Hitachi High-Tech Corporation, Tokyo, Japan) equipped with a 1 cm quartz cuvette.

The presence of hydroxyl radicals (•OH) was measured by electron paramagnetic resonance spectroscopy (ESR, Bruker, Germany) with 50 mM of DMPO taken as a spin-trapping agent. Lastly, high-performance liquid chromatography-mass spectrometry (HPLC-MS, Agilent 1290/6460, USA) with a linear ion trap interface and a quaternary pump was used to analyse the degradation intermediates of ciprofloxacin.

3. Results and discussion

3.1 Beads characterization.

Fe_2O_3@MOF beads have been successfully prepared by *in situ* (Fe_2O_3) and two-step (Fe_2O_3) routes as shown in Figure 1. Both materials exhibited morphological and highly magnetic responsiveness, which allowed them to be separated quickly in an external magnetic field. Two traditional methods of preparation were used to prepare Fe_2O_3@MOF microspheres. In the case of *in situ* method (Figure 1A), the mixed solution of chitosan with iron precursor ions was dropwise into an alkaline coagulation bath, and the *in situ* precipitation of iron species took place (Eq (2)) [31], [38]. The process facilitated the development of nanoscale domains of iron oxide and their uniform inclusion into the MOF-like porous structure to form Fe_2O_3 MOF beads. In the case of the two-step approach (Figure 1B), the Fe_2O_3 nanoparticles were synthesized by a two-step synthesis method, which includes the hydrothermal synthesis of Fe_2O_3 nanoparticles at 200 °C for 8 h using $FeCl_3 \cdot 6H_2O$, sodium acetate, polyethylene glycol and ethylene glycol, followed by washing and drying. The resultant nanoparticles were then added to a chitosan solution and turned into porous Fe_2O_3@MOF beads by alkaline coagulation. The in-situ route, however, produced Fe_2O_3 nanoparticles in situ in the porous matrix formed by chitosan during bead formation, leading to a more uniform dispersion of nanoparticles and increased interaction between the nanoparticles and the porous structure. The obtained beads were very magnetic and were easily retrieved from aqueous solution with an external magnetic field (Figure 1C) or purchased directly (Figure 1D). Moreover, as illustrated in Figures 1E and 1F, prepared Fe_2O_3@MOF beads could be quickly trapped using an external magnet, which implies that they are highly magnetic responsive and can be separated with ease. These structural findings suggest that the method of synthesis has a strong effect on nanoparticle dispersion and pore structure.

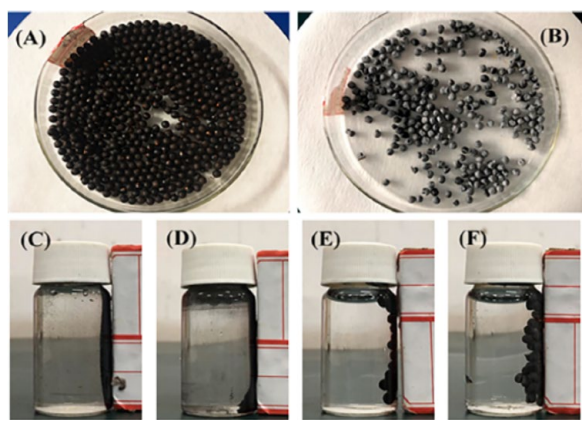

Figure 1: Digital photographs showing the appearance and magnetic response of Fe_2O_3@MOF beads prepared by different synthesis routes: (a) beads obtained by the *in situ* synthesis method, (b) beads obtained by the two-step synthesis method, (c) synthesized Fe_2O_3 nanoparticles, (d) commercial Fe_2O_3 nanoparticles, and magnetic separation of Fe_2O_3@MOF beads prepared by (e) *in situ* and (f) two-step methods.

SEM analysis (Figure 2A–C) indicated that Fe_2O_3@MOF-IS had a more regular and inter-linked porous structure than Fe_2O_3@MOF-TS. TEM analysis revealed that Fe_2O_3 nanoparticles in Fe_2O_3@MOF-IS were well dispersed with an

average size of around 6.1 nm, whereas the particles were significantly larger (around 170.5 nm) in Fe_2O_3@MOF-TS. SEM and TEM were used to study the morphologies and microstructures of the as-prepared beads.

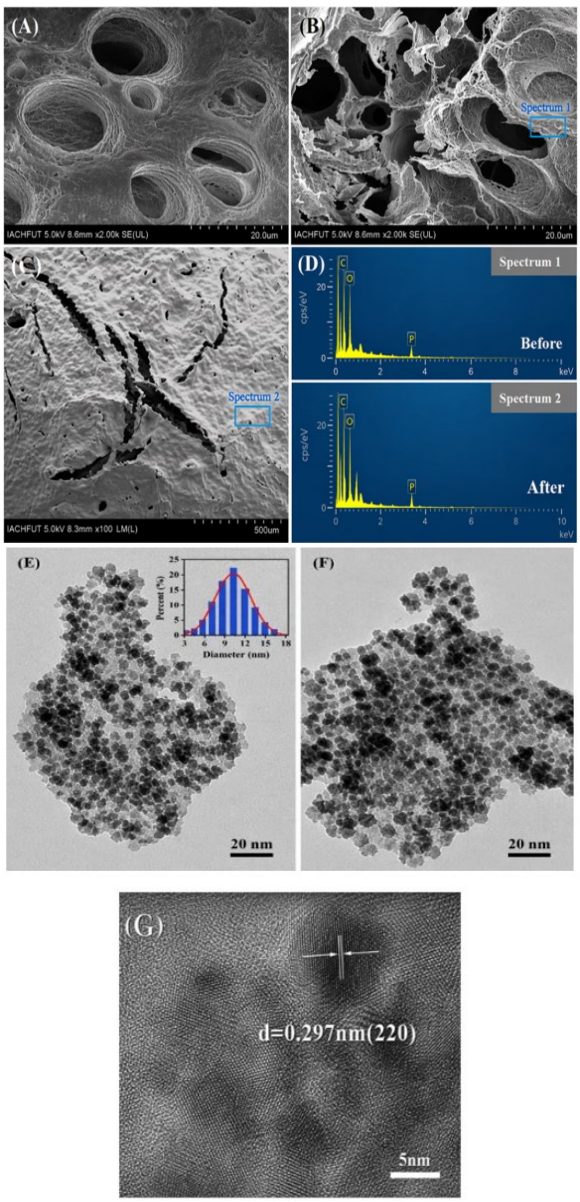

Figure 2: Morphological characterization of Fe_2O_3@MOF beads: SEM images of (a) two-step beads, (b) *in situ* beads before reaction, and (c) after reaction; (d) EDS spectrum; (e, f) TEM images (inset: particle size distribution); and (g) HRTEM image showing lattice fringes.

The SEM image of the two-step Fe_2O_3@MOF in Figure 2A had less uniform and bigger pore systems than *in situ* Fe_2O_3@MOF beads in Figure 2B, and should therefore offer a greater number of access sites to H_2O_2 diffusion, greater exposure of active sites on the catalyst, and facilitated electron and ion transport. Following the reaction (Figure 2C), small cracks and blocked pores appeared on the bead surface, which could affect long-term recyclability. Moreover, the EDS analysis (Figure 2D) proved the existence of C, O, N, and Fe in the beads before and after reaction, but the percentage of Fe reduced a bit (20.2 to 19.3), which indicates that little iron was lost during the catalytic reaction.

TEM images of the *in situ* beads (Figure. 2E, F) indicated that the large domains of nanoscale iron oxide of a mean diameter of about 6.10 nm were uniformly distributed on the surface of the beads, meaning that the supporting framework inhibited nanoparticle agglomeration effectively. In comparison, the mean size of the particles of the two-step beads was much larger (approximately 170.5 nm) and probably decreased the active surface area and catalytic efficiency. Separation between lattice fringes was measured at 0.296 nm (Figure. 2G) in agreement with the respective crystalline plane of iron oxide [37]. In the meantime, the distribution of C, Fe, and O on the bead surface was examined using elemental mapping, which proved it to be homogeneous.

The XRD was used to determine the phase structures of the pristine and composite beads prepared through both methods (Figure 3A). All the samples exhibited the characteristic diffraction peaks of iron oxide, which means that the formation of the magnetic iron-based component has been successful [37]. These peaks could be indexed with the corresponding standard card (JCPDS 75-0033), which proves that the produced iron oxide phase was well crystallized. Also, the synthesis and integration of the polymeric framework into the composite beads was identified by the existence of a widely dispersed amorphous peak (2) in Figure. 3A (c-g). It is worth noting that the used beads showed the same diffraction peaks as the fresh beads, indicating that the catalyst crystalline structure was not disrupted in the course of the reaction, thus supporting good reusability.

Applied Science and Engineering Progress, Vol. 20, No. 3, 2027, 8280

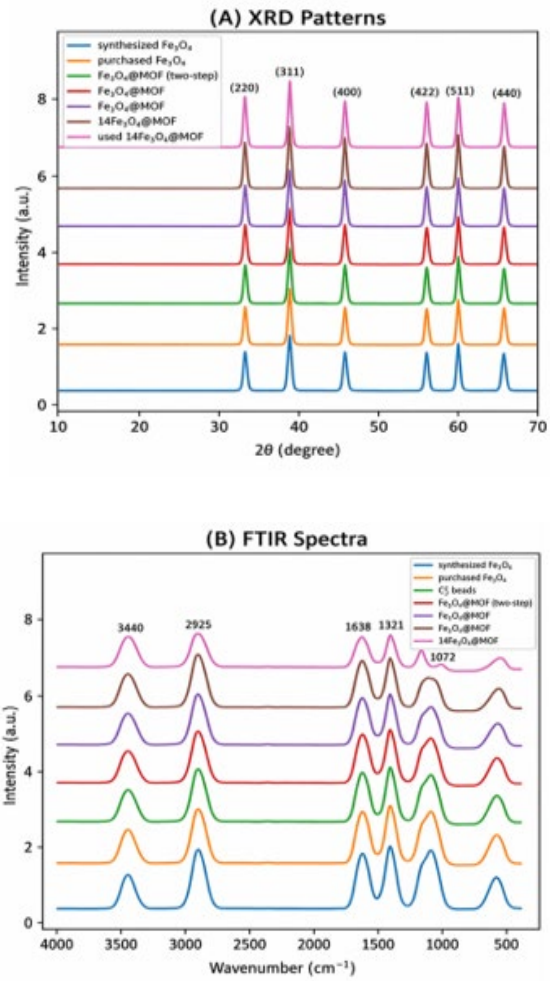

Figure 3: Structural characterization of Fe_2O_3@MOF beads: (a) XRD patterns and (b) FT-IR spectra.

FT-IR spectra (Figure. 3B) served as one more confirmation of the formation of the composite structure. The stretching vibration of OH and NH groups in the matrix produced by chitosan was broad and at 3440 cm^{-1}. The bands at 1648 and 1595 cm^{-1} were attributed to NH vibrations, whereas the peaks at 1421 and 1379 cm^{-1} were attributed to CO groups of remaining acetylated groups [39]. Other absorption bands at 1031, 1074 and 1151 cm^{-1} were in line with the saccharide structures [39]. Notably, the presence of iron oxide in the beads was also established by the iron-oxygen vibration band in the region near 570 cm^{-1}, which is in line with the XRD findings. As the iron loading increased, the FeO band was increasingly broadened and the NH band was slightly shifted, indicating that metal NH_2 interactions were formed [40], [41].

The XPS analysis was conducted to explain surface chemical states further (Figure 4A–D). The wide-scan spectrum (Figure. 4A) revealed that the beads were mainly C, O, N, and Fe, and the atomic contents of these elements were about 41.2, 29.1, 5.6 and 21.4, respectively, which were also in line with the EDS results. C1s spectrum (Figure. 4B) deconvolution showed that there were C–C, C–O–C, and C=O at the frequencies of 284.8, 286.4, and 288.0 eV, respectively. In the O_1s spectrum (Figure. 4C), the lattice oxygen peak was located at around 529.6 eV and the peaks around 531.2 and 532.8 eV were considered to be surface hydroxyl oxygen and C–O related oxygen species [42], [43]. Fe_{2p} spectrum (Figure. 4D) revealed a mixed-valence iron complex, and thus, the presence of Fe^{2+} and Fe^{3+} complexes, and satellite peaks [44]. All these findings indicate the successful synthesis of Fe_2O_3@MOF composites.

Thermal stability was measured by TGA analysis (Figure. 4E). Similar weight loss behaviour in multisteps was observed in both the clean chitosan matrix and Fe_2O_3@MOF beads. The initial phase (25–200 °C) was associated with evaporation of moisture. The second phase (200–320 °C) was connected with the degradation of polymer chains (deacetylation/ depolymerization). Carbonization was done in the third stage (>320 ºC) and carbon was left behind. Further weight-loss characteristics in higher temperatures were explained by reactions between iron oxide and carbonaceous residues [45]. In general, the thermal stability of the incorporation of iron oxide was better than that of the neat polymer matrix. The XPS analysis confirmed the coexistence of both Fe^{2+} and Fe^{3+} species on the surface of Fe_2O_3@MOF catalysts, which suggests the presence of a mixed-valence iron system that is highly favorable for the heterogeneous Fenton-like reactions. The simultaneous presence of Fe^{2+} and Fe^{3+} allows for the continuous electron transfer between neighbouring iron centers, which helps to accelerate the Fe^{2+}/Fe^{3+} redox cycle, responsible for the activation of H_2O_2 and the formation of hydroxyl radicals. This leads to a mixed-valence surface composition, which gives it a large number of catalytically active sites for the oxidation of H_2O_2, generating highly reactive oxygen species, which are responsible for the oxidation of ciprofloxacin [46].

The surface areas and porosity were obtained from the N_2 adsorption-desorption isotherms and shown in Figure. 4F. The isotherms were of type IV

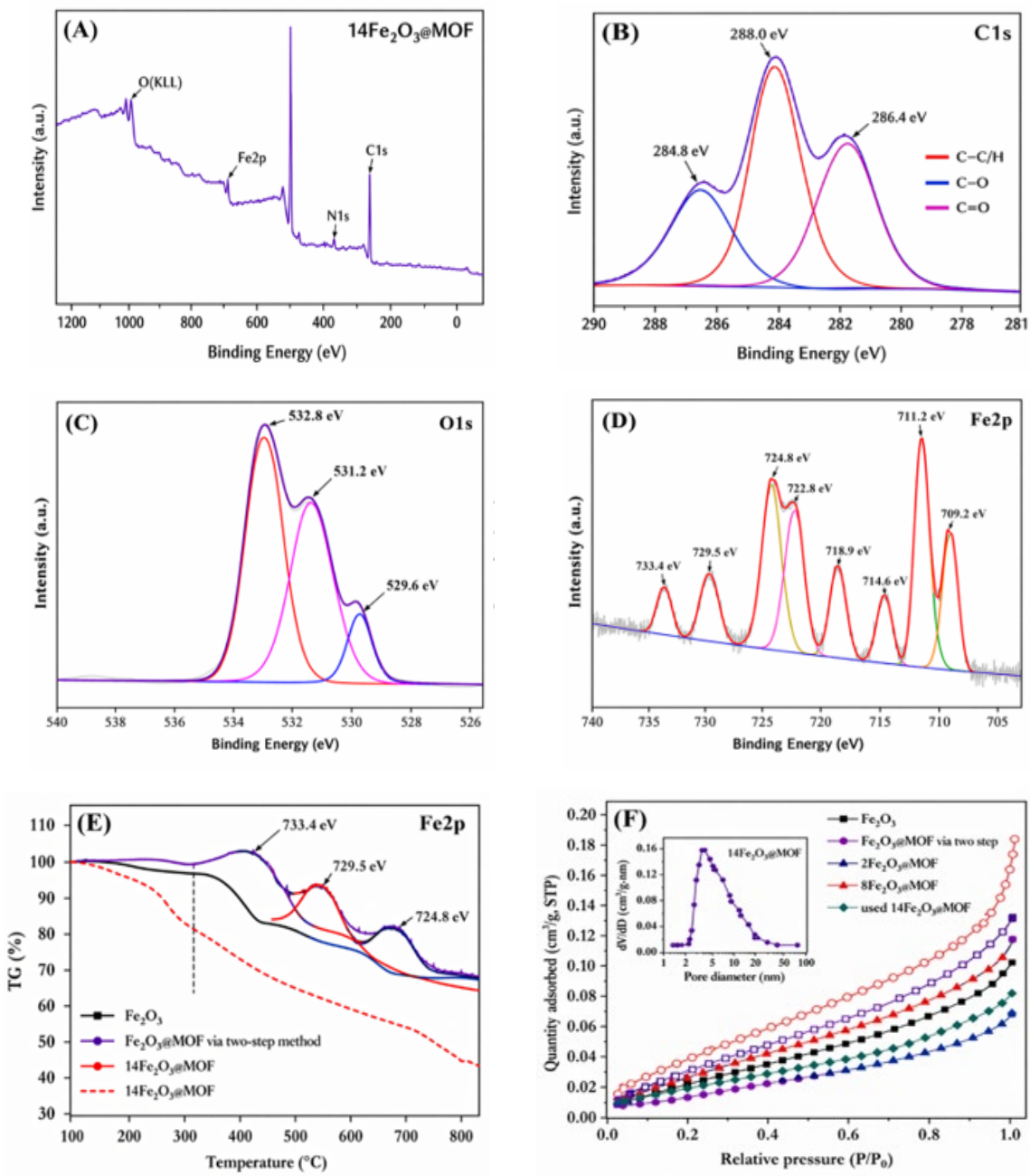

Figure 4: Surface chemistry, thermal stability, and porosity of Fe_2O_3@MOF beads: XPS spectra of (a) survey, (b) C1s, (c) O1s, and (d) Fe2p; (e) TGA curves; and (f) N_2 adsorption–desorption isotherms with corresponding pore size distribution (inset).

and the H3 hysteresis loop was formed according to IUPAC, which shows that the morphology of the produced mesoporous structures was slit-shaped. The surface area of the iron oxide beads synthesized from the two-step method was less than that of the iron oxide *in situ* bead that was synthesized in the same

Applied Science and Engineering Progress, Vol. 20, No. 3, 2027, 8280

manner. The decrease in surface area of the iron oxide in-situ bead could have been attributed to the partial blocking of pores during the synthesis of the iron oxide beads by the formation of iron oxide. Interestingly, 14Fe_2O_3@MOF beads lost only 19.8 m^2 g^{-1}, indicating that there was minimal degradation of the porous structure after the reaction. A summary of detailed porosity parameters is given in Table 1. The pore size distribution (inset of Figure. 4F) corresponded to the presence of mesopores (immediately) around a size of 4 nm and a wide distribution, which is similar to BJH analysis [47].

The structural properties developed during the synthesis path greatly influence the catalytic activity of the Fe_2O_3@MOFs beads. The in-situ synthesized catalyst showed the Fe_2O_3 nanoparticles with the average diameter of ~ 6.1 nm, while the two-step synthesized catalyst showed large nanoparticles of ~ 170.5 nm. The relatively small particle size leads to a higher density of surface iron atoms and a more uniform distribution of active sites in the porous matrix, which ensures good contact between H_2O_2 and catalytic Fe centers. Even if the incorporation of finely dispersed Fe_2O_3 nanoparticles slightly reduced the BET surface area and pore volume due to partial pore occupation, the increased dispersion of the Fe_2O_3 nanoparticles and increased number of active sites in the pores compensated for this and resulted in more efficient activation of H_2O_2 and more rapid Fe^{2+}/Fe^{3+} redox cycling. Furthermore, the homogeneous distribution of iron overcomes the problem of aggregation of nanoparticles and decreases the diffusion limitation, which leads to a higher apparent pseudo-first-order rate constant for the degradation of ciprofloxacin than the two-step synthesized catalyst. The results presented here show that the dispersion of the nanoparticles and the accessibility of the active sites are much more significant factors in determining the catalytic activity than their surface area alone, emphasizing the importance of synthesis-route engineering to optimize the catalytic activity of heterogeneous Fenton catalysts.

3.2 Catalytic activity of prepared catalysts via two different synthesis routes

CIP degradation was used to compare the catalytic activity of Fe_2O_3@MOF-IS and Fe_2O@MOF-TS (Figure 5A). Fe_2O_3@MOF-IS has demonstrated much faster degradation, as it reached a degradation of approximately 93.4 % after 25 min, compared to Fe2O3@MOF-TS, which took a significantly longer reaction time. By extension, Fe_2O_3@MOF–IS was also found to remove more TOC (~66.5%) and leach less iron (0.72 ± 0.06 mg L^{-1}) than Fe_2O_3@MOF–TS (2.55 ± 0.14 mg L^{-1}), which implied greater stability and mineralization capacity. These findings clearly illustrate that the synthesis route significantly influences the physicochemical properties of the catalyst, which in turn determine its catalytic performance. The Fe_2O_3/H_2O_2 system of ciprofloxacin (CIP) degradation (initial CIP concentration 0.095 mM, -44.5 mg L^{-1}) was done on the catalytic activities of beads synthesized using both methods. The *in situ* 14Fe_2O_3 beads on MOF also led to rapid degradation of CIP and as illustrated in Figure. 5A, the *in situ* beads (Figure. 5A) removed CIP more rapidly, with 93.8% being removed in less time than the two-step beads (Figure. 5A) with a similar iron loading. The two-step beads that were loaded with bought nanoparticles were even less active (Figure. 5A). The *in situ* system was found to stabilize at a maximum removal of about 93.4% at around 25 min and the two-step beads took several hours to stabilize.

The system of *in situ* beads/H_2O_2 quickly and nearly fully decomposed H_2O_2 in 110-120 min, in comparison to the two-step beads, where H_2O_2 was only partially decommissioned in the same time. The

Table 1: Characteristics of Fe_2O_3@MOF catalysts made through *in situ* and two-step syntheses, such as BET surface area, pore volume, and average pore diameter.

Sample	Fe (mmol/10 mg catalyst)	BET Area (m^2 g^{-1})	Pore Volume (cm^3 g^{-1})	Pore Diameter (nm)
in situ synthesis				
MOF beads	0	49.87	0.075	3.42
2Fe_2O_3@MOF	0.0081 ± 0.0005	31.76	0.058	3.79
8Fe_2O_3@MOF	0.0261 ± 0.0010	23.86	0.061	3.61
14Fe_2O_3@MOF	0.0409 ± 0.0007	21.08	0.053	3.79
Used 14Fe_2O_3@MOF	0.0396 ± 0.0005	19.82	0.049	3.62
Two-step synthesis				
Fe_2O_3@MOF-TS	0.0415 ± 0.0003	56.74	0.126	3.27

increased TOC reduction also proved better mineralization capacity: the in-situ beads demonstrated a better removal of TOC, about 66.5 % in 110 -120 min, which is obviously greater than that of the two-step beads. Further, iron leaching was measured, and it was found to be more stabilized: the leached iron concentration of two-step beads (2.55 - 0.14 mg L^{-1}) was approximately three and four times greater than that of the *in situ* beads (0.72 - 0.06 mg L^{-1}) after 110-120 min, which are better structured materials [18].

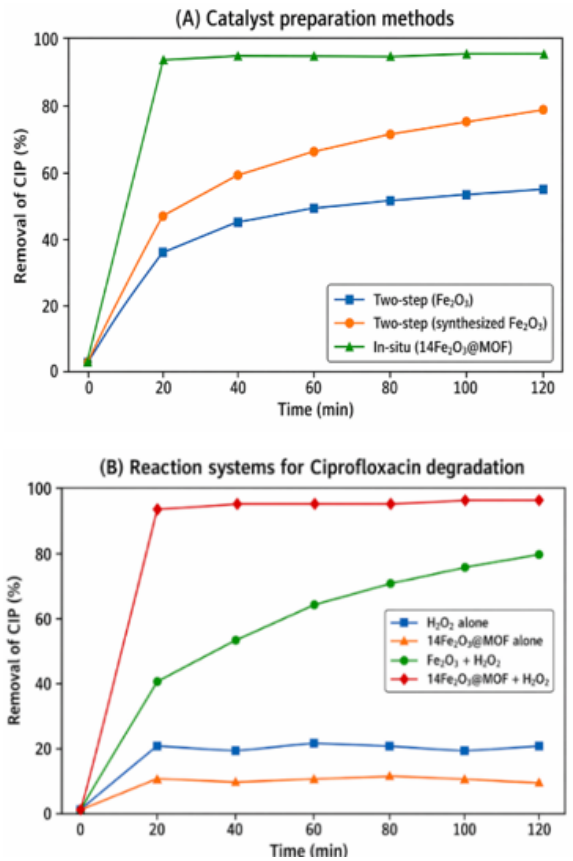

Figure 5: Catalytic performance of Fe_2O_3@MOF beads: (a) comparison of ciprofloxacin (CIP) degradation using catalysts prepared by different synthesis methods; (b) CIP degradation under different reaction systems.

The apparent increase in catalytic activity of an *in situ* method is primarily due to: (i) the greater number of active sites being exposed in that iron oxide species are preferentially formed and anchored at the surface/porous interface and not encapsulated; and (ii) much smaller particle size of iron oxide crystal in in-situ beads (~6.10 nm) than in two step beads (~170.5 nm) which results in larger effective surface area and enhanced activation of H_2O_2 [35]. Thus, *in situ* synthesized Fe_2O_3@MOF beads were chosen to be used in further experiments.

3.3 Fenton-like catalytic activities of Fe_2O_3@MOF beads.

In order to determine the catalytic performance of *in situ* synthesized Fe_2O_3 beads under the influence of H_2O_2, the batch experiments were carried out in various reaction systems (Figure. 5B). The removal of CIP was low in the H_2O_2-only system (about 19.3 per cent), which implied that H_2O_2 does not have a strong direct oxidation of CIP in the absence of a catalyst. With the system comprising only catalysts, CIP degradation was observed at a relatively low rate of only 10.1%, mostly through adsorption onto the porous beads.

This adsorption mechanism is associated with the mesoporous network that offers available cavities and channels to facilitate solid-liquid interaction [21]. Conversely, CIP degradation in the Fe_2O_3@MOF/H_2O_2 system was significantly enhanced and it took about 25 minutes to get about 93-93.4% of CIP degraded. The enhanced performance can be explained by the synergistic effect of the iron-based active sites and the porous MOF-derived framework, preventing the agglomeration of nanoparticles and supporting effective electron transfer to active H_2O_2. As a result, a significant volume of hydroxyl radicals (•OH) is produced to oxidize ciprofloxacin [26], [48]. Recent reports on antibiotic degradation with different types of Fenton-like catalysts are summarized in Table 2, and it can be seen that the prepared Fe_2O_3@MOF beads had high degradation efficiency in a short period with competitive utilization efficiency of the H_2O_2.

3.4 Effects of experimental factors on the breakdown of ciprofloxacin.

3.4.1 Influences of iron in catalyst.

Catalytic efficiency is directly proportional to the number of surface active sites (iron species) [49]. In order to explore this effect, the content of iron in the beads with various loadings was measured using ICP-MS following an acid digestion (Table 2). Figure. 6A

Table 2: Comparison of the catalytic performance of Fe_2O_3@MOF-1S with other heterogeneous Fenton-like catalysts reported to degrade ciprofloxacin (CIP) under different operating conditions.

Catalyst	CIP_0 (mg L^{-1})	Removal (%)	H_2O_2 (mM)	Time (min)	H_2O_2 Consumption (mol g^{-1} CIP)	Ref.
$MnFe_2O_4$/Biochar	42	94.2	100	120	2.58	[26]
Fe_3O_4@C	22	78.6	5	120	0.305	[27]
Fe@*Bacillus subtilis*	18	92.4	380	100	16.95	[28]
MIL-100(Fe)@Fe_3O_4/CA	12	83.7	10	180	1.12	[29]
Fe_2O_3@MOF beads (This work)	45.5	93.4	10	25	0.221	This work

shows how much CIP degradation per 25 min was enhanced as a result of increasing iron content (per 10 mg catalyst) within the 0.0082 to 0.0409 mmol range; it was found that the rate of the reaction was greatly influenced by iron loading. Increased loading of iron offers increased active sites and facilitates the activation of H_2O_2 (Table 2). Thus, the sample with the most significant loading (14Fe_2O_3 in MOF) was chosen for further experiments.

The *in situ* synthesized Fe_2O_3@MOF beads show a superior catalytic performance that can be directly related to the physicochemical properties. The TEM images revealed that the *in situ* synthesized Fe_2O_3 nanoparticles had an average diameter of around 6.1 nm, while the two-step synthesized Fe_2O_3 catalyst had a much larger average diameter of around 170.5 nm. The catalytic active sites are uniformly distributed in the porous framework with a much higher external surface area in the case of the significantly smaller *in situ* generated nanoparticles. The moderate BET surface-area and pore-volume decrease after partial pore filling with finely dispersed Fe_2O_3 did, however, significantly enhance the accessibility of active sites, and the activation efficiency of H_2O_2 was significantly higher due to the intimate contact between the Fe_2O_3 nanoparticles and the supporting matrix. Also, the uniform distribution of iron and the proper loading of iron enabled rapid redox cycling of Fe^{2+} to Fe^{3+}, while simultaneously minimizing aggregation of the nanoparticles and leaching of the iron. This result showed that the *in situ* synthesized catalyst had a higher apparent degradation rate constant than the two-step synthesized catalyst, indicating that dispersion of nanoparticles and accessibility of active sites is a more important factor for the catalytic activity than is only the BET surface area.

3.4.2. Effects of pH

The solution pH has an impact on the surface charge, adsorption dynamics, and electron transfer, influencing Fenton-like activity [50]. With the increase of pH between 3 and 7 (Figure 6B), the CIP degradation between 110 and 120 min fell drastically by approximately 94.0 to 27.8, showing intense pH dependence. Iron species also prefer to have a hydrated form, and the catalytic power reduces at pH above 4 [51]. Additionally, H_2O_2 decomposes into oxygen more readily than it forms highly oxidizing hydroxyl radicals (•OH) in nearly neutral and alkaline conditions (pH > 5), which means it is less efficient at oxidation. Most iron-based Fenton and Fenton-like catalysts display the best efficiency at a pH of approximately 3.0 [52], [53], at which Fe^{2+}/Fe^{3+} redox cycling and activation of H_2O_2 are the most efficient. Even though the pH level was 4.0 (which is still in the acidic region), the Fe_2O_3@MOF beads exhibited relatively high catalytic activity at this pH, which shows that the catalyst has good catalytic activity even under mild acid conditions. This behavior implies enhanced operational flexibility compared to the normal heterogeneous (homo-Fenton) systems, which usually have a steeper pH activity profile.

3.4.3. Effects of H_2O_2 concentration

Figure. 6C displays the effect of H_2O_2 concentration. In the absence of H_2O_2, a smaller percentage of CIP was removed (around 11% in the next 110-120 minutes), whereas a larger percentage of CIP was degraded with the increase of H_2O_2 (5-10 mM) (around 46.0 to 72.3 percent in the next 25 minutes). Nevertheless, at H_2O_2 beyond 10 mM, the efficiency of degradation slowed slightly because of excess H_2O_2 scavenging, resulting in reduced reactive $HO_2.O_2$ radicals [54] (Eqs. (3 - 5):

$$H_2O_2 + \bullet OH \rightarrow HO_2\cdot + H_2O \quad (3)$$

$$HO_2\cdot + \bullet OH \rightarrow H_2O + O_2 \quad (4)$$

$$\bullet OH + \bullet OH \rightarrow H_2O_2 \quad (5)$$

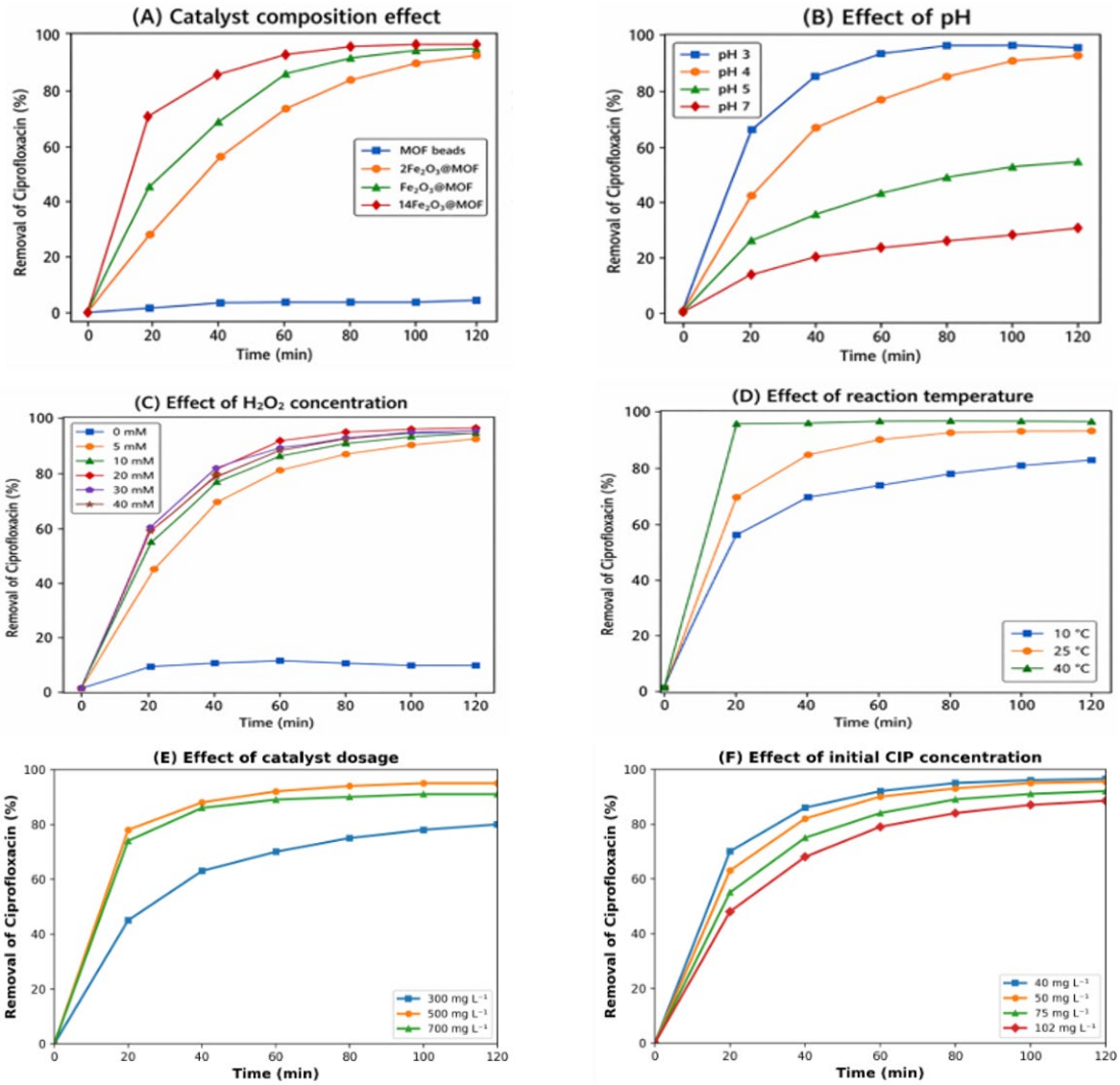

Figure 6: Influence of different operational parameters on the degradation of Ciprofloxacin (CIP) under Fe_2O_3@MOF-catalyzed Fe_2O_3 mFenton-like:(a) catalyst iron content in Fe_2O_3@MOF, (b) initial pH, (c) H_2O_2 concentration, (d) temperature, (e) catalyst dosage, (f) CIP concentration.

3.4.4. Reaction temperature effects

Effects of temperature were assessed at 10 ° C, 25 °C and 40 °C (Figure. 6D). The temperature enhanced the degradation of CIP. As an illustration, CIP degradation during 110-120 min was about 86.0, 94.0 and 94.6 at 10, 25 and 40 °C, respectively. Even though the temperature marginally increased the rates, the variation between 25 and 40 °C was minimal; hence, given the real-world wastewater circumstances, 25 °C was chosen to use in the subsequent experiments.

3.4.5. Effects of catalyst dosage

Catalyst dosage (300 to 700 mg L^{-1}) was found to have a severe influence on CIP degradation (Figure. 6E). The rate of CIP degradation in 25 min went up to approximately 63.0 to approximately 93.8 percent as dosage rose by 300 to 500 mg L^{-1}. A further addition of dosage to 700 mg L^{-1}, however,

had a minor negative effect on the CIP degradation (89.2% in 25 min), presumably because overabundant radicals started to self-quench, since the lifetime of •OH is very short [55]. The most important reactions are presented in the following equations (Eqs. (6) - (8)):

$$Fe^{3+} + H_2O_2 \rightarrow Fe^{2+} + HO_2\cdot + H^+ \quad (6)$$

$$Fe^{2+} + H_2O_2 \rightarrow Fe^{3+} + \bullet HO + H^- \quad (7)$$

$$\bullet HO + \bullet H \rightarrow H_2O_2 \quad (8)$$

The pseudo-first-order kinetic model (Eq. (9)) was applied:

$$ln(C_0/C) = Kt \quad (9)$$

where C_0 and C_t (mg L^{-1}) represent the CIP concentrations at initial time and at reaction time t (min), respectively, and k (min^{-1}) is the apparent rate constant.

As shown in Figure. 6, a linear relationship between $\ln(C_0/C_t)$ and time was observed, confirming that the degradation process follows pseudo-first-order kinetics (Table 3). The rate constant (k) of Fe_2O_3@MOF is much greater than that of Fe_2O_3@MOF-TS which implies that the *in situ* synthesized catalyst has higher catalytic activity. This is due to the fact that the dispersion of Fe_2O_3 nanoparticles is enhanced, the active sites are more accessible, and the activation of H_2O_2 occurs more efficiently.

Table 3: Apparent pseudo-first-order kinetic constants for ciprofloxacin degradation under different experimental conditions.

Experimental condition	Variable	k (min^{-1})	R^2
Synthesis route	Fe_2O_3@MOF-IS	0.112	0.996
	Fe_2O_3@MOF-TS	0.065	0.993
Catalyst dosage	300 mg L^{-1}	0.041	0.991
	500 mg L^{-1}	0.112	0.996
	700 mg L^{-1}	0.097	0.994
H_2O_2 concentration	5 mM	0.056	0.992
	10 mM	0.112	0.996
	25 mM	0.095	0.991
Initial pH	3.0	0.112	0.996
	4.0	0.079	0.993
Initial CIP concentration	40 mg L^{-1}	0.126	0.995
	50 mg L^{-1}	0.112	0.996
	102 mg L^{-1}	0.058	0.992

Moreover, the rate constant rose as the concentration of H_2O_2 and dosage of catalysts increased, as more reactive oxygen species were formed, whereas high levels of H_2O_2 resulted in a minor decline in k, presumably because of scavenging. At excessive H_2O_2 concentrations, however, H_2O_2 itself becomes a radical scavenger, consuming hydroxyl radicals:

$$H_2O_2 + \cdot OH \rightarrow HO_2^{\cdot} + H_2O$$

which decreases the concentration of active radicals and slightly lowers the observed k. In the same manner, high rate constants were favored by acidic conditions, which is in line with increased redox cycling of Fe^{2+}/Fe^{3+} in acidic conditions.

3.4.6. Influences of starting CIP concentration.

The real pharmaceutical wastewater can contain tens to hundreds of mg L^{-1} level of antibiotics [56]. Thus, concentrations of CIP 0.09-0.23 mM (approximately 40-102 mg L^{-1}) were studied. Within this concentration range, over 88 per cent of CIP could be degraded in 110-120 min, indicating a well-performing catalyst as shown in Figure. 6F. The rate constant dropped as CIP concentration increased, probably because of competitive adsorption of CIP and H_2O_2 and the concentration of intermediates that prevent the access of the H_2O_2 to the active sites. The catalyst was nonetheless able to treat high CIP loads effectively as compared with the past studies [26]-[29].

3.5 Decomposition of 14Fe_2O_3@MOF ciprofloxacin.

Applicability of 14Fe_2O_3@MOF in practical terms was also tested based on the degradation of ciprofloxacin with an initial concentration of about 45-50 mg L^{-1} [57]. As Figure 7A demonstrates, the breakdown of ciprofloxacin was more than 95 percent in 110-120 minutes. The kinetics of degradation is demonstrated in Figure. 7B that takes the form of pseudo-first-order with a rate constant of k 0.032 min^{-1} that indicates a healthy catalytic oxidation process.

3.6 Stability and reusability of 14Fe_2O_3@MOF beads.

The stability and reusability of catalysts are significant in the practical applications of wastewater. There was a total of six reuse cycles (Figure 8A). Beads were collected at the end of each run by magnetism and then freeze-dried over 24 h. More than 84% of CIP remained degraded within 110-120 min after six cycles, which is also evidence of excellent recyclability. The percentage of TOC degradation dropped to an average of 51.0 percent, as compared to 66.5 percent, following the sixth cycle, and this is a moderate decrease, yet indicating high mineralization.

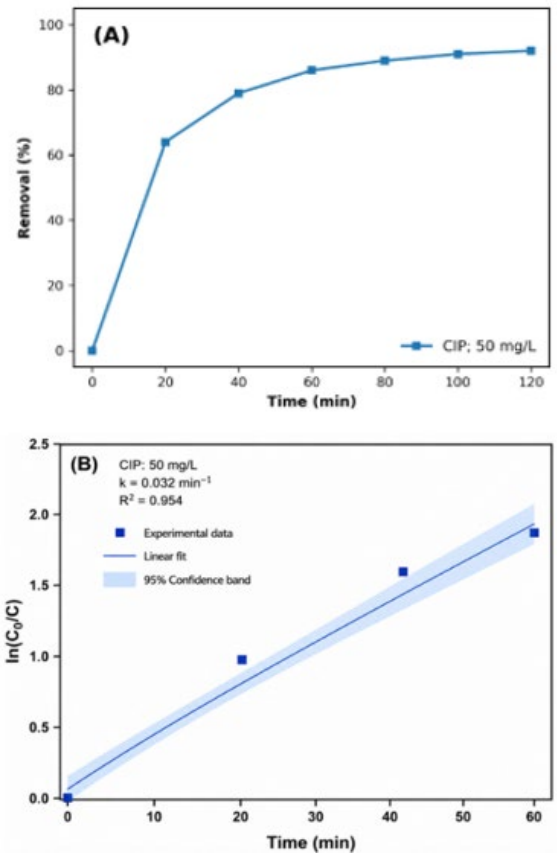

Figure 7: Degradation efficiency and kinetic analysis of ciprofloxacin (CIP). (a) CIP degradation efficiency as a function of reaction time. (b) Pseudo-first-order kinetic plot for CIP degradation under optimized conditions. Reaction conditions: pH 3.0, initial CIP concentration 50 mg/L, catalyst dosage 500 mg/L, H_2O_2 concentration 10 mM, and temperature 25 °C.

Further confirmation came about as a result of iron leaching. The amount of $14Fe_2O_3$ in the $14Fe_2O_3$@MOF was approximately 115 mg L^{-1}. The washed iron reduced slowly (approximately, 0.72-0.23) to 0.23 mg L^{-1} in subsequent cycles (Figure. 8B). The leached iron during the first cycle was about 0.72 mg L^{-1} and it was only about 0.63 percent of the total amount of iron. This stability has been explained by the high binding/anchoring of iron species into the porous structure [58], which inhibits leaching and aggregation. Hence, it can be concluded that Fe_2O_3@MOF beads are highly promising in terms of their use in water treatment.

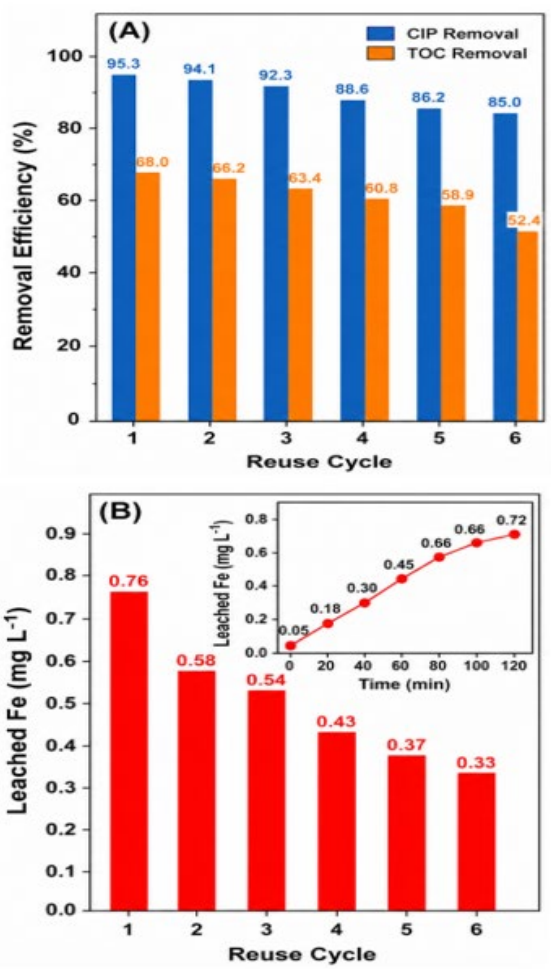

Figure 8: Six successive cycles of degradation and reusability of the $14Fe_2O_3$@MOF beads under catalytic conditions. (a) Ciprofloxacin (CIP) degradation efficiency and total organic carbon (TOC) degradation efficiency over six reuse cycles. After every reaction cycle, (b) the leaching of iron; inset is the change in dissolved iron concentration after the first reaction cycle. Reaction conditions: initial concentration of CIP was 50.09 mg L^{-1}, the amount of catalyst was 500 mg L^{-1}, the concentration of H2O2 was 10 mM, the initial pH was 3.0, the reaction temperature was 25 °C, and the reaction time was 120 min per cycle.

The Fe_2O3@MOF catalyst was found to be an effective catalyst for removing ciprofloxacin (CIP), with a removal efficiency of approximately 93%, but the total organic carbon (TOC) removal was not as high, around 66%, suggesting that the removal of the parent molecule CIP does not necessarily mean

full mineralization. This heterogeneous Fenton-like reaction starts to generate a series of lower molecular weight oxidation intermediates of ciprofloxacin by attacking with hydroxyl radicals, and then the intermediates are slowly oxidized and mineralized. So, under the conditions investigated the observed catalytic process mainly reflects efficient degradation of the parent pollutant with partial mineralisation, rather than complete mineralisation to CO_2 and H_2O.

3.7 Ciprofloxacin degradation reaction pathways

3.7.1. Dynamic process of CIP degradation

UV-vis spectra taken during the degradation of CIP (200-500 nm) are presented in Figure 9. The typical absorption maximum of ciprofloxacin close to 276-278 nm slowly declined and came to the baseline values after approximately 80-90 minutes, which implied that ciprofloxacin was heavily degraded. In the meantime, variations in the UV area indicated that the conjugated structure was destroyed and assembled into intermediate fragments. The temporary rise in absorbance in the 230-240 nm zone at the beginning of the 60 minutes of the experiment suggests the appearance of intermediate products and their further breakdown. In the present work, several degradation intermediates were detected during the heterogeneous Fenton-like process for the oxidation of ciprofloxacin, but their biological toxicity was not investigated. Not all the transformations of pharmaceuticals are detoxifying, and some oxidation intermediates can have antibacterial activity or other ecotoxicological characteristics than the parent compound. It can be concluded that the suggested degradation pathway shows that the structure of the ciprofloxacin has been changed efficiently and partially mineralized to other substances, but more studies with a toxicity test or computational toxicity prediction should be conducted to assess the safety of the formed intermediates in the environment and to ensure the complete mineralization of the treated wastewater.

The reaction conditions were as follows: pH 3.0 initially; CIP, 50.09 mg L^{-1}; catalyst, 500 mg L^{-1}; H_2O_2, The reaction condition was as follows: pH 3.0; initially CIP, 50.09 mg L^{-1}; catalyst, 500 mg L^{-1}; H_2O_2.The reaction condition was as follows: pH 3.0; initially CIP, 50.09 mg L^{-1}; catalyst 110 mM; temperature, 25 °C).

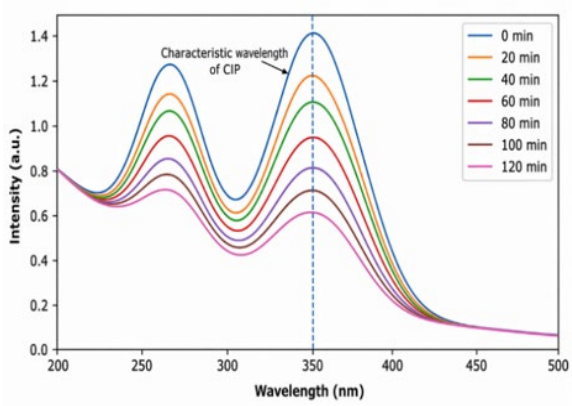

Figure 9: UV–vis absorption spectra recorded during CIP degradation over 14Fe_2O_3@MOF.

3.7.2. Intermediate degradation analysis of CIP

Ciprofloxacin was significantly mineralized in the Fe_2O_3@MOF/H_2O_2 system, as shown by the outcome of the TOC (reduction of about 66.5%). HPLC–MS was used to identify the intermediates of degradation and several fragment ions were observed. According to the identified intermediates and to the available literature data concerning the oxidation of ciprofloxacin, a series of probable transformation pathways was suggested [59], [60]. Overall, degradation of ciprofloxacin occurs (i) by cleavage/transformation of functional groups (e.g. oxidation of the piperazine ring), (ii) defluorination, hydroxylation and (iii) ring opening of aromatic rings, ultimately resulting in the formation of small organic acids and inorganic end products [61], [62].

3.8. Fenton-like degradation pathway

Hydroxyl radicals (•OH) are the most commonly recognised reactive species in heterogeneous Fenton-like systems [63]. In order to confirm this, radical quenching experiments were conducted with tert-butanol, KI, and p-benzoquinone. For instance, tert-butanol quenches both surface-generated and free •OH radicals KI scavenges mainly the surface-adsorbed radicals, and p-benzoquinone is employed to scavenge superoxide-related species [64]-[66]. The significant reduction in the degradation of CIP after addition of tert-butanol and KI suggested that •OH radicals play a primary role in the degradation of CIP, while the lower inhibition extent by p-benzoquinone indicated a partial contribution of other reactive oxygen species.

Applied Science and Engineering Progress, Vol. 20, No. 3, 2027, 8280

The four-line signal was observed in the Fe_2O_3 system in the presence of H_2O_2 with the 1:2:2:1 intensity ratio in the ESR measurements with the DMPO (Figure 10B), confirming the generation of •OH radicals, but no significant peaks were found in the control system.

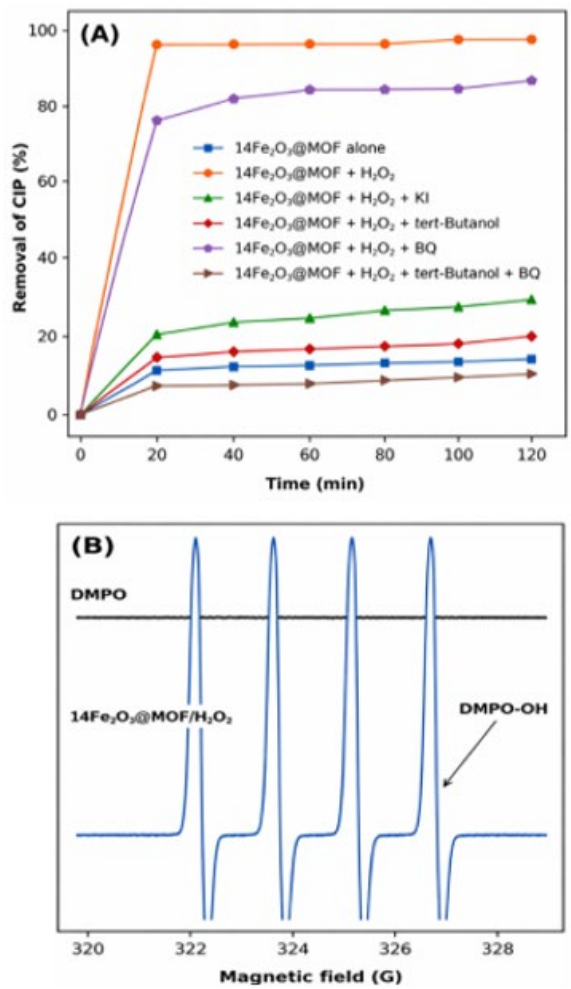

Figure 10: Radical scavengers on degradation of CIP (a). ESR spectra of DMPO-OH adducts, which were produced during the time period with Fenton-like degradation of a suspension of $14Fe_2O_4$@MOF/H_2O_2 (b). (Reaction conditions: pH 3.0; catalyst, 500 mg L^{-1}; H_2O_2, 10 mM; temperature, 25 C).

Collectively, these results suggest that subsequently, upon loading CIP and H_2O_2, both compounds can be enriched into the porous structure in which the beads of the Fe_2O_3@MOF are embedded. In the first step, CIP is adsorbed on the bead surface via electrostatic and π-π interactions. Once H_2O_2 is added, Fe-based active sites catalyze the decomposition of H_2O_2 to produce surface-adsorbed •OH radicals that oxidize CIP through several electron-transfer reactions. The heterogeneous pathway predominates, although minor iron leaching may also lead to solution oxygen-generating •OH radicals. The improved catalytic activity originates from an efficient electron transport between the Fe^{2+}/Fe^{3+} pair and the porous skeleton [67].

The reactions may be formulated as (Eqs. (10) to (17)) shown below:

$$Fe^{2+} + H_2O_2 \rightarrow Fe^{3+} + \bullet OH\_surf + OH^- \quad (10)$$

$$Fe^{3+} + H_2O_2 \rightarrow Fe^{2+} + HO_2\bullet\_surf + H^+ \quad (11)$$

$$Fe^{3+} + H_2O_2\bullet\_surf \rightarrow Fe^{2+} + O_2 + H^+ \quad (12)$$

$$\bullet OH\_surf + CIP \rightarrow CO_2 + H_2O \quad (13)$$

$$Fe^{2+} + H_2O_2 \rightarrow Fe^{3+} + \bullet OH\_free + OH^- \quad (14)$$

$$Fe^{3+} + H_2O_2 \rightarrow Fe^{2+} + HO_2\bullet\_free + H^+ \quad (15)$$

$$Fe^{3+} + H_2O_2\bullet\_free \rightarrow Fe^{2+} + O_2 + H^+ \quad (16)$$

$$\bullet OH\_free + CIP \rightarrow CO_2 + H_2O \quad (17)$$

Radical scavenging experiments and electron spin resonance (ESR) were used to study the catalytic process by which ciprofloxacin (CIP) is degraded over Fe_2O_3@MOF-IS. CIP degradation was inhibited strongly by the addition of tert-butanol (OH scavenger), which shows that hydroxyl radicals (•OH) are the most reactive species. Conversely, p-benzoquinone (O_2 - scavenger) was found to have a relatively lesser inhibitory action, which indicated a secondary effect of superoxide radicals. ESR spectra also identified the formation of •OH radicals by the typical DMPO-OH signals, which gave direct evidence of the formation of reactive oxygen species in the Fenton-like process.

The proposed degradation pathway indicates that hydroxylation reactions, piperazine ring opening reactions, decarboxylation and defluorination reactions are the initial reactions in which hydroxyl radicals react with the ciprofloxacin molecule to produce a series of intermediate products. During the heterogeneous Fenton-like process, these intermediates further oxidize, which leads to partial mineralization, as shown in the TOC removal results. The mineralization to CO_2 and H_2O was not completed under the conditions of the present experiment.

Structural differences induced during the synthesis, in addition to the presence of the Fe_2O_3 nanoparticles, are believed to be the source of the superior catalytic performance of the *in situ*-synthesized Fe_2O_3@MOF beads [66]. The *in situ* route can achieve uniform dispersion of nanoparticles in a porous matrix, better interaction between Fe_2O_3 and the supporting framework, and better exposure of the active sites of catalysis. Due to these structural properties, the activation of H_2O_2 is promoted, Fe^{2+}/Fe^{3+} redox cycling is accelerated, aggregation of nanoparticles is suppressed and iron leaching is reduced, which leads to a higher efficiency of the degradation of the antibiotic ciprofloxacin compared with the conventional synthesis route with two steps [52].

All of these improvements in the catalytic performance of the in-situ synthesized Fe_2O_3@MOF beads are closely related to the smaller size of the nanoparticles, the homogeneous distribution of Fe, the improved accessibility of the active site, the efficient redox cycling of Fe^{2+}/Fe^{3+}, and the higher apparent degradation rate constant, revealing that the synthesis-route engineering is of paramount importance in optimizing the heterogeneous Fenton-like catalysts. According to such results, the degradation process can be explained by the Fe^{2+}/Fe^{3+}redox cycle on the catalyst surface, which activates H_2O_2 and results in the formation of the radical OH. Fe_2O_3@MOF is better performing because of its smaller particle size, better dispersion, and better interfacial contact, which allows an effective transfer of electrons and continuous regeneration of the active sites. The formed •OH radicals also quickly oxidize CIP molecules into intermediate products, which are further mineralized to CO_2 and H_2O, as supported by the results of TOC degradation.

4 Conclusion

The present study shows that the physicochemical properties and catalytic activity of Fe_2O_3@MOF beads in the degradation process of ciprofloxacin (CIP) in the presence of $FeCl_3$ are strongly dependent on the synthesis method. The *in situ* approach led to catalysts featuring a more homogeneous distribution of nanoparticles, better accessibility of active sites, higher catalytic activation of H_2O_2, reduced leaching of Fe, and higher catalytic activity. The results are useful in understanding the synthesis-route engineering as a viable method to develop optimized heterogeneous Fenton catalysts for pharmaceutical wastewater treatment. The reaction performance is significantly influenced by the operational parameters, which include iron loading, pH, H_2O_2 dosage, catalyst dosage and initial pollutant concentration. CIP degradation occurred primarily via reactive hydroxyl radicals (•OH) produced by redox cycling of Fe^{2+}/Fe^{3+} ions; mechanistic studies confirmed this finding. Importantly, the bead structure facilitated magnetic recovery, enabled excellent reusability with low iron leaching and sustained catalytic activity over several successive cycles. In summary, the results indicate that the synthesis route is crucial in directing catalyst structure and activity, and that the Fe_2O_3@MOF-IS is beneficial for application potential in treating pharmaceutical wastewater.

Acknowledgments

The authors gratefully acknowledge their respective institutions for the academic and technical support provided during the completion of this research. This research received no external funding.

Author Contributions

M.A.K.: conceptualization, methodology, investigation, formal analysis, data curation, visualization, and writing—original draft; S.A.-A.: methodology, investigation, validation, and resources; K.H.K.: formal analysis, data curation, validation, and visualization; O.A.A.: conceptualization, supervision, project administration, methodology, and writing—review and editing; R.N.A.-M.: validation, resources, and writing—review and editing. All authors have read and agreed to the published version of the manuscript.

Conflicts of Interest

The authors declare no conflict of interest.

Declaration of generative AI and AI-assisted technologies in the writing process

The authors declare that no generative AI or AI-assisted technologies were used in the preparation, writing, or editing of this manuscript.

References

[1] F. Deng, L. N. Zhao, X. B. Luo, S. L. Luo, and D. D. Dionysiou, “Highly efficient visible-light photocatalytic performance of Ag/$AgIn_5S_8$ for degradation of tetracycline hydrochloride and

treatment of real pharmaceutical industry wastewater," *Chemical Engineering Journal*, vol. 333, pp. 423–433, 2018, doi: 10.1016/j.cej. 2017.09.160.

[2] Y. Zhou et al., "Research progress on adsorption behavior and mechanism of antibiotics in soil," *Ecology and Environment*, vol. 32, no. 11, pp. 2072–2082, Nov. 2023, doi: 10.16258/j.cnki.1674-5906.2023.11.018.

[3] J. Sun et al., "Enhanced oxytetracycline removal coupling with increased power generation using a self-sustained photo-bioelectrochemical fuel cell," *Chemosphere*, vol. 221, pp. 21–29, 2019, doi: 10.1016/j.chemosphere.2019.01.027.

[4] S. Hu, Y. Zhang, G. Shen, H. Zhang, Z. Yuan, and W. Zhang, "Adsorption/desorption behavior and mechanisms of sulfadiazine and sulfamethoxazole in agricultural soil systems," *Soil and Tillage Research*, vol. 186, pp. 233–241, Mar. 2019, doi: 10.1016/j.still.2018.10.016.

[5] M. Wei, D. Lv, L. Cao, K. Zhou, and K. Jiang, "Adsorption behaviours and transfer simulation of levofloxacin in silty clay," *Environmental Science and Pollution Research*, vol. 28, no. 34, pp. 46291–46302, Sep. 2021, doi: 10.1007/s11356-021-13734-2.

[6] J. Y. Cao, L. D. Lai, B. Lai, G. Yao, X. Chen, and L. P. Song, "Degradation of tetracycline by peroxymonosulfate activated with zero-valent iron: Performance, intermediates, toxicity and mechanism," *Chemical Engineering Journal*, vol. 364, pp. 45–56, 2019, doi: 10.1016/j.cej.2019.01.146.

[7] Z. Guo, K. P. Cui, G. M. Zeng, J. J. Wang, and X. P. Guo, "Silver nanomaterials in the natural environment: An overview of their biosynthesis and kinetic behavior," *Science of the Total Environment*, vol. 643, pp. 1325–1336, 2018, doi: 10.1016/j.scitotenv.2018.06.256.

[8] Y. H. Chen et al., "High-throughput profiling of antibiotic resistance gene dynamics in a drinking water river-reservoir system," *Water Research*, vol. 149, pp. 179–189, 2019, doi: 10.1016/j.watres. 2018.11.016.

[9] J. Wan et al., "Rhamnolipid stabilized nano-chlorapatite: Synthesis and enhancement effect on Pb and Cd immobilization in polluted sediment," *Journal of Hazardous Materials*, vol. 343, pp. 332–339, 2018, doi: 10.1016/j.jhazmat.2017. 09.042.

[10] H. F. Xiong, D. L. Zou, D. D. Zhou, S. S. Dong, J. W. Wang, and B. E. Rittmann, "Enhancing degradation and mineralization of tetracycline using intimately coupled photocatalysis and biodegradation," *Chemical Engineering Journal*, vol. 316, pp. 7–14, 2017, doi: 10.1016/j.cej. 2017.01.050.

[11] W. Wang, Z. Nan, W. Kong, Y. Jiang, and Y. Wu, "Enhanced adsorption and leaching behavior of fluoroquinolone antibiotics in soil amended with cattle manure under varying rainfall condition," *Journal of Environmental Chemical Engineering*, vol. 13, no. 3, p. 116831, Jun. 2025, doi: 10.1016/j.jece.2025.116831.

[12] S. Lv et al., "Competitive adsorption and desorption of three antibiotics in distinct soil aggregate size fractions," *Ecotoxicology and Environmental Safety*, vol. 259, p. 115002, Jul. 2023, doi: 10.1016/j.ecoenv.2023.115002.

[13] X. Jiang, Y. H. Guo, L. B. Zhang, W. J. Jiang, and R. Z. Xie, "Catalytic degradation of tetracycline hydrochloride by persulfate activated with nano Fe^0 immobilized mesoporous carbon," *Chemical Engineering Journal*, vol. 341, pp. 392–401, 2018, doi: 10.1016/j.cej.2018.02.101.

[14] A. Abdurahman, S. Li, Y. Li, X. Song, and R. Gao, "Ecotoxicological effects of antibiotic adsorption behavior of microplastics and its management measures," *Environmental Science and Pollution Research*, vol. 30, no. 60, pp. 125370–125387, Dec. 2023, doi: 10.1007/s11356-023-30987-5.

[15] Z. M. Liu, M. F. Zhu, Z. Wang, H. Wang, C. Deng, and K. Li, "Effective degradation of aqueous tetracycline using a nano-TiO_2/carbon electrocatalytic membrane," *Materials*, vol. 9, p. 364, 2016, doi: 10.3390/ma9050364.

[16] R. P. Rietra, B. J. Berendsen, Y. Mi-Gegotek, P. F. Römkens, and A. M. Pustjens, "Prediction of the mobility and persistence of eight antibiotics based on soil characteristics," *Heliyon*, vol. 10, no. 1, Jan. 2024, doi: 10.1016/j.heliyon.2024.e23845.

[17] W. Ma et al., "Single and ternary competitive adsorption-desorption and degradation of amphenicol antibiotics in three agricultural soils," *Journal of Environmental Management*, vol. 297, Art. no. 113366, 2021, doi: 10.1016/j.jenvman.2021.113366.

[18] R. L. Liu, Y. M. Xu, and B. L. Chen, "Self-assembled nano-FeO(•OH)/reduced graphene oxide aerogel as reusable catalyst for photo-Fenton

degradation of phenolic organics," *Environmental Science & Technology*, vol. 52, pp. 7043–7053, 2018, doi: 10.1021/acs.est. 8b01103.

[19] X. Deng, Y. Jiang, M. A. Zhang, Z. Nan, X. Liang, and G. Wang, "Sorption properties and mechanisms of erythromycin and ampicillin in loess soil: Roles of pH, ionic strength, and temperature," *Chemical Engineering Journal*, vol. 434, Art. no. 134694, 2022, doi: 10.1016/j.cej.2022.134694.

[20] H. Zhu, J. He, Y. Wu, L. Tong, W. Zhang, and L. Zhuang, "Assessment of global antibiotic exposure risk for crops: Incorporating soil adsorption via machine learning," *Environmental Science & Technology*, vol. 58, no. 30, pp. 13327–13336, Jul. 2024, doi: 10.1021/acs.est.4c02123.

[21] J. T. Tang and J. L. Wang, "Fenton-like degradation of sulfamethoxazole using Fe-based magnetic nanoparticles embedded into mesoporous carbon hybrid as efficient catalyst," *Chemical Engineering Journal*, vol. 351, pp. 1085–1094, 2018, doi: 10.1016/j.cej.2018.06.146.

[22] D. L. Jiang, T. Y. Wang, Q. Xu, D. Li, S. C. Meng, and M. Chen, "Perovskite oxide ultrathin nanosheets/g-C_3N_4 2D–2D heterojunction photocatalysts with enhanced activity for tetracycline photodegradation," *Applied Catalysis B: Environmental*, vol. 201, pp. 617–628, 2017, doi: 10.1016/j.apcatb. 2016.08.045.

[23] R. S. Ribeiro, A. M. T. Silva, J. L. Figueiredo, J. L. Faria, and H. T. Gomes, "Catalytic wet peroxide oxidation: Hybrid magnetic carbon nanocomposites for degradation of organic pollutants," *Applied Catalysis B: Environmental*, vol. 187, pp. 428–460, 2016, doi: 10.1016/j.apcatb. 2016.01.019.

[24] M. Cheng, G. M. Zeng, D. Huang, C. Lai, P. Xu, C. Zhang, and Y. Liu, "Hydroxyl radicals-based advanced oxidation processes for remediation of soils contaminated with organic compounds: A review," *Chemical Engineering Journal*, vol. 284, pp. 582–598, 2016, doi: 10.1016/j.cej.2015.08.173.

[25] Y. Sun, Z. X. Yang, P. F. Tian, Y. Y. Sheng, J. Xu, and Y. F. Han, "Oxidative degradation of nitrobenzene by Fenton-like reaction with Fe–Cu bimetallic catalysts," *Applied Catalysis B: Environmental*, vol. 244, pp. 1–10, 2019, doi: 10.1016/j.apcatb.2018.11.003.

[26] C. Lai et al., "Magnetic $MnFe_2O_4$/biochar composite and heterogeneous photo-Fenton degradation of tetracycline at near-neutral pH," *Chemosphere*, vol. 224, pp. 910–921, 2019, doi: 10.1016/j.chemosphere.2019.02.121.

[27] B. Kakavandi, A. Takdastan, N. Jaafarzadeh, M. Azizi, A. Mirzaei, and A. Azari, "Application of Fe_3O_4@C catalyzing heterogeneous UV-Fenton system for tetracycline removal with RSM optimization," *Journal of Photochemistry and Photobiology A*, vol. 314, pp. 178–188, 2016, doi: 10.1016/j.jphotochem.2015.08.015.

[28] M. Conde-Cid et al., "Adsorption/desorption of three tetracycline antibiotics on different soils in binary competitive systems," *Journal of Environmental Management*, vol. 262, p. 110337, May 2020, doi: 10.1016/j.jenvman. 2020.110337.

[29] H. U. Rasheed, X. M. Lv, S. Y. Zhang, W. Wei, N. Ullah, and J. M. Xie, "MIL-100(Fe)@Fe_3O_4/CA magnetic nanophotocatalysts for Fenton-like degradation of tetracycline," *Advanced Powder Technology*, vol. 29, pp. 3305–3314, 2018, doi: 10.1016/j.apt.2018.09.008.

[30] Q. Song et al., "Selective adsorption behavior/mechanism of antibiotic contaminants on novel boron nitride bundles," *Journal of Hazardous Materials*, vol. 364, pp. 654–662, Feb. 2019, doi: 10.1016/j.jhazmat.2018.10.070.

[31] R. Soumaya, A. Amrane, F. Fourcade, A. Assadi, L. Monser, and N. Adhoum, "Electro-Fenton catalyzed with magnetic chitosan beads for removal of Chlordimeform insecticide," *Applied Catalysis B: Environmental*, vol. 226, pp. 346–359, 2018, doi: 10.1016/j.apcatb.2017. 12.063.

[32] X. Xu et al., "Adsorption/desorption and degradation of doxycycline in three agricultural soils," *Ecotoxicology and Environmental Safety*, vol. 224, Art. no. 112675, 2021, doi: 10.1016/j.ecoenv.2021.112675.

[33] K. Wang et al., "Insights into behavior and mechanism of tetracycline adsorption on virgin and soil-exposed microplastics," *Journal of Hazardous Materials*, vol. 440, Art. no. 129770, 2022, doi: 10.1016/j.jhazmat.2022.129770.

[34] K. X. Wang et al., "Hybrid porous magnetic bentonite-chitosan beads for selective removal of radioactive cesium in water," *Journal of Hazardous Materials*, vol. 362, pp. 160–169, 2019, doi: 10.1016/j.jhazmat.2018.09.041.

[35] M. A. Huiting, J. Li, F. Li, and C. H. Liang, "Adsorption–desorption interaction characteristics

of ammonium nitrogen and typical antibiotics in soil," *Rock and Mineral Analysis*, vol. 44, no. 5, pp. 911–925, May 2025, doi: 10.15898/j.cnki.11-2131/td.2025. 05.012.

[36] Y. Chen, C. Hu, D. Deng, Y. Li, and L. Luo, "Factors affecting sorption behaviors of tetracycline to soils: Importance of soil organic carbon, pH and Cd contamination," *Ecotoxicology and Environmental Safety*, vol. 197, Art. no. 110572, Jul. 2020, doi: 10.1016/j.ecoenv.2020.110572.

[37] Z. J. Yan et al., "Pulverization control by confining Fe_3O_4 nanoparticles individually into macropores of hollow carbon spheres for high-performance Li-ion batteries," *ACS Applied Materials & Interfaces*, vol. 10, pp. 2581–2590, 2018, doi: 10.1021/acsami.7b17021.

[38] Z. Guo, G. M. Zeng, K. P. Cui, and A. W. Chen, "Toxicity of environmental nanosilver: Mechanism and assessment," *Environmental Chemistry Letters*, vol. 17, pp. 319–333, 2019, doi: 10.1007/s10311-018-0783-9.

[39] J. Ding, X. Duan, L. Tong, W. Chen, Z. Zhang, and Q. Shi, "Study of the adsorption behavior of multiple antibiotics at the water–sediment interface," *Water, Air, & Soil Pollution*, vol. 236, no. 10, Art. no. 660, 2025, doi: 10.1007/s11270-025-06760-2.

[40] J. Wu, H. Zeng, F. Meng, Y. Zhao, D. Li, and J. Zhang, "In situ construction of metal–phenolic networks in chitosan/polyvinyl alcohol hydrogel beads for efficient tetracycline hydrochloride removal with recyclability from complex water systems," *Separation and Purification Technology*, Art. no. 136567, Dec. 2025, doi: 10.1016/j.seppur.2025.136567.

[41] L. Weerasundara, Y. S. Ok, P. Kumarathilaka, A. Marchuk, and J. Bundschuh, "Assessment and optimization of As(V) adsorption on hydrogel composite integrating chitosan-polyvinyl alcohol and Fe_3O_4 nanoparticles and evaluation of their regeneration and reusable capabilities in aqueous media," *Science of the Total Environment*, vol. 855, Art. no. 158877, Jan. 2023, doi: 10.1016/j.scitotenv.2022.158877.

[42] Q. Song, J. Gao, Y. Lin, Z. Zhang, and Y. Xiang, "Synthesis of cross-linking chitosan-PVA composite hydrogel and adsorption of Cu(II) ions," *Water Science and Technology*, vol. 81, no. 5, pp. 1063–1070, Mar. 2020, doi: 10.2166/wst.2020.160.

[43] P. Zhang et al., "A biomass resource strategy for alginate-polyvinyl alcohol double network hydrogels and their adsorption to heavy metals," *Separation and Purification Technology*, vol. 301, Art. no. 122050, Nov. 2022, doi: 10.1016/j.seppur.2022.122050.

[44] X. Liu et al., "Morphology-dependent activation of hydrogen peroxide with Cu_2O for tetracycline hydrochloride degradation in bicarbonate aqueous solution," *Journal of Environmental Sciences*, vol. 137, pp. 567–579, Mar. 2024, doi: 10.1016/j.jes.2023.08.021.

[45] C. F. Zheng et al., "Modified magnetic chitosan microparticles as novel superior adsorbents for capturing food dyes," *Journal of Hazardous Materials*, vol. 367, pp. 492–503, 2019, doi: 10.1016/j.jhazmat.2018.12.065.

[46] T. J. Jiang et al., "Oxygen doped graphitic carbon nitride nanosheets for the degradation of organic pollutants by activating hydrogen peroxide in the presence of bicarbonate in the dark," *RSC Advances*, vol. 11, no. 1, pp. 296–306, 2021, doi: 10.1039/D0RA08994A.

[47] F. J. Ariza-Pineda, I. F. Macías-Quiroga, D. F. Hinojosa-Zambrano, J. D. Rivera-Giraldo, D. M. Ocampo-Serna, and N. R. Sanabria-González, "Treatment of textile wastewater using the $Co(II)/NaHCO_3/H_2O_2$ oxidation system," *Heliyon*, vol. 9, no. 12, Dec. 2023, doi: 10.1016/j.heliyon.2023.e22534.

[48] Y. J. Yao et al., "Iron encapsulated in boron and nitrogen codoped carbon nanotubes as synergistic catalysts for Fenton-like reaction," *Water Research*, vol. 101, pp. 281–291, 2016, doi: 10.1016/j.watres.2016.05.083.

[49] E. G. Garrido-Ramirez, J. F. Marco, N. Escalona, and M. S. Ureta-Zanartu, "Preparation and characterization of bimetallic Fe–Cu allophane nanoclays and their activity in phenol oxidation by heterogeneous electro-Fenton reaction," *Microporous and Mesoporous Materials*, vol. 225, pp. 303–311, 2016, doi: 10.1016/j.micromeso.2016.01.012.

[50] Q. Xia et al., "Activation of H_2O_2–HCO_3^- by $Ca_2Co_2O_5$ for pollutant degradation," *Environmental Science and Pollution Research*, vol. 31, no. 35, pp. 48450–48459, Jul. 2024, doi: 10.1007/s11356-024-34567-8.

[51] J. Huang, C. Puyang, and H. Guo, "Sodium percarbonate activation by plasma-generated ozone for catalytic degradation of dye wastewater: Role of active species and

degradation process," *Catalysts*, vol. 12, no. 7, p. 681, Jun. 2022, doi: 10.3390/catal12070681.

[52] L. He et al., "Highly efficient degradation of emerging contaminants with sodium bicarbonate-enhanced Mn(II)/peracetic acid process: Formation and contribution of Mn(V)," *Environmental Science & Technology*, vol. 58, no. 45, pp. 20313–20326, Nov. 2024, doi: 10.1021/acs.est.4c04567.

[53] W. Zhong and J. L. Wang, "Degradation of sulfamethazine using Fe_3O_4–Mn_3O_4/reduced graphene oxide hybrid as Fenton-like catalyst," *Journal of Hazardous Materials*, vol. 324, pp. 653–664, 2017, doi: 10.1016/j.jhazmat.2016. 11.040.

[54] R. L. Rizalmen, L. Alrozi, and N. A. Zubir, "Bicarbonate-activated hydrogen peroxide in presence of $Ca_{0.5}Fe_{0.5}O_3$ perovskite for highly efficient carbamazepine degradation," *Archives of Metallurgy and Materials*, pp. 211–217, 2025, doi: 10.24425/amm.2025.148765.

[55] J. Wang et al., "In situ incorporation of iron-copper bimetallic particles in electrospun carbon nanofibers as an efficient Fenton catalyst," *Applied Catalysis B: Environmental*, vol. 207, pp. 316–325, 2017, doi: 10.1016/j.apcatb.2017.02.021.

[56] Y. H. Chen et al., "Environmental media exert a bottleneck in driving the dynamics of antibiotic resistance genes in modern aquatic environment," *Water Research*, vol. 162, pp. 127–138, 2019, doi: 10.1016/j.watres.2019. 06.045.

[57] N. A. Urbina-Suarez, C. J. Salcedo-Pabón, G. L. López-Barrera, J. B. García-Martínez, A. F. Barajas-Solano, and F. Machuca-Martínez, "Using response surface methodology to treat tannery wastewater with the bicarbonate–peroxide system," *ChemEngineering*, vol. 7, no. 4, Art. no. 62, Jul. 2023, doi: 10.3390/chemen gineering7040062.

[58] Z. Guo, W. D. Ding, X. W. Liu, Z. Sun, and L. Wei, "Two-dimensional black phosphorus: A new star in energy applications and the barrier to stability," *Applied Materials Today*, vol. 14, pp. 51–58, 2019, doi: 10.1016/j.apmt.2018. 11.006.

[59] H. R. Dong et al., "Removal of tetracycline by Fe/Ni bimetallic nanoparticles in aqueous solution," *Journal of Colloid and Interface Science*, vol. 513, pp. 117–125, 2018, doi: 10.1016/j.jcis.2017.10.082.

[60] W. X. Wang, K. J. Xiao, L. Zhu, Y. R. Yin, and Z. M. Wang, "Graphene oxide-supported titanium dioxide and ferroferric oxide hybrid: A magnetically separable photocatalyst with enhanced photocatalytic activity for tetracycline hydrochloride degradation," *RSC Advances*, vol. 7, pp. 21287–21297, 2017, doi: 10.1039/C7RA01855A.

[61] Y. Chai, Y. Cai, Y. Guan, H. Ai, and Z. Yang, "Enhanced degradation of organic dye in aqueous solutions by bicarbonate-activated hydrogen peroxide with a rosin-based copper catalyst," *Journal of Water Process Engineering*, vol. 66, Art. no. 106035, Sep. 2024, doi: 10.1016/j.jwpe.2024.106035.

[62] K. Y. Mora-Bonilla, I. F. Macías-Quiroga, N. R. Sanabria-González, and M. T. Dávila-Arias, "Bicarbonate-activated hydrogen peroxide for an azo dye degradation: Experimental design," *ChemEngineering*, vol. 7, no. 5, Art. no. 86, Sep. 2023, doi: 10.3390/chemengineering7050086.

[63] N. A. Urbina-Suarez et al., "Bicarbonate-hydrogen peroxide system for treating dyeing wastewater: Degradation of organic pollutants and color removal," *Toxics*, vol. 11, no. 4, Art. no. 366, Apr. 2023, doi: 10.3390/toxics11040366.

[64] X. Zhang, J. Wang, X. X. Dong, and Y. K. Lv, "Functionalized metal-organic frameworks for photocatalytic degradation of organic pollutants in environment," *Chemosphere*, vol. 242, Art. no. 125144, Mar. 2020, doi: 10.1016/j.chemosphere.2019.125144.

[65] T. Xia, Y. Lin, W. Li, and M. Ju, "Photocatalytic degradation of organic pollutants by MOFs-based materials: A review," *Chinese Chemical Letters*, vol. 32, no. 10, pp. 2975–2984, Oct. 2021, doi: 10.1016/j.cclet.2021.03.028.

[66] D. Chen et al., "Photocatalytic degradation of organic pollutants using TiO_2-based photocatalysts: A review," *Journal of Cleaner Production*, vol. 268, p. 121725, Sep. 2020, doi: 10.1016/j.jclepro.2020.121725.

[67] X. Qin, K. Zhao, X. Quan, P. Cao, S. Chen, and H. Yu, "Highly efficient metal-free electro-Fenton degradation of organic contaminants on a bifunctional catalyst," *Journal of Hazardous Materials*, vol. 416, Art. no. 125859, Aug. 2021, doi: 10.1016/j.jhazmat.2021.125859.